Engineering Fracture Mechanics 195 (2018) 279–296

Contents lists available at ScienceDirect

Engineering Fracture Mechanics

journal homepage: www.elsevier.com/locate/engfracmech

Fracture toughness testing using non-standard bend specimens – Part I: Constraint effects and development of test procedure

Vitor S. Barbosa, Claudio Ruggieri*

Department of Naval Architecture and Ocean Engineering, University of São Paulo, São Paulo, Brazil

ARTICLE INFO

Keywords:
Fracture toughness test
3-point bend specimens
4-point bend specimens
J-integral
CTOD
Plastic area
Plastic hinge model

ABSTRACT

This work addresses the development of a fracture toughness test procedure using standard and non-standard SE(B) specimens, including non-standard 4-point bend configurations. In the present study, extensive plane-strain finite element analyses are conducted on non-standard bend geometries with varying specimen span over width ratio (S/W) and loaded under 3-point and 4-point bending. The potential influence of specimen geometry and loading on fracture behavior in terms of $J-Q$ descriptions to quantify constraint effects is characterized first. Next, a large new set of plastic η-factors applicable to these non-standard bend geometries which serve to estimate the experimentally measured toughness values in terms of load-displacement records, including the *J*-integral and the crack tip opening displacement (CTOD), is provided. To facilitate contact with other test protocols, a new set of rotational factors, r_p, to determine the CTOD based on the plastic hinge model is also described. The extensive numerical analyses conducted here provide a large set of fracture toughness test parameters, which not only validate the existing relationships available in current standards, but also provide support to standardization efforts for fracture toughness testing using non-standard bend geometries.

1. Introduction

Standardized testing programs to measure cleavage fracture toughness in metallic alloys, including ferritic steels in the ductile-to-brittle transition (DBT) region, routinely employ three-point bend, SE(B), or compact tension, C(T), specimens containing deep, through cracks $(a/W \gtrsim 0.45–0.5)$ to insure predominantly plane-strain, small-scale yielding (SSY) conditions at the crack tip coupled with a highly constrained bending field acting on the remaining crack ligament. Under such conditions, a single parameter described by the *J*-integral (or, equivalently, the crack tip opening displacement, CTOD or δ, and elastic-plastic stress intensity factor, K_J), uniquely scales the elastic-plastic near-tip fields thereby providing a fully characterization of the local conditions leading to unstable (cleavage) fracture (see, e.g., the review by Hutchinson [1]). Fracture toughness testing standards, such as ASTM E1820 [2] and ASTM E1921 [3], thus guarantee that the corresponding critical values of these fracture parameters, such as the *J*-integral at cleavage instability, J_c, or K_{Jc}, define lower bound, geometry independent measures of cleavage fracture toughness. Simplified engineering approaches for defect assessments, including BS7910 [4] and API579 [5], also referred to as engineering critical assessment (ECA) procedures, rely on the direct application of these toughness measures to provide conservative predictions of structural integrity for in-service components containing crack-like flaws. Very similar arguments also hold in the case of experimental measurements of crack growth resistance properties, as characterized by the increase in *J*-integral over the first few mm of stable crack extension (Δa), for ductile materials. Here, testing standards for resistance curves (such as ASTM E1820 [2]) also employ deeply cracked specimens

* Corresponding author.
E-mail address: claudio.ruggieri@usp.br (C. Ruggieri).

https://doi.org/10.1016/j.engfracmech.2018.03.029
Received 6 January 2018; Received in revised form 22 March 2018; Accepted 26 March 2018
Available online 05 April 2018

such as the near-tip region of elastic unloading and nonproportional loading is well contained within the J-dominance zone thereby insuring stable crack growth under J-controlled conditions [1].

Paralleling these concepts, there has been renewed interest in the use of small (subsize) specimens to measure fracture toughness properties for safety and material degradation assessments of critical structural components. The primary impetus to this activity has been the need of the commercial fusion reactor industry to assess effects of neutron irradiation on material toughness degradation on reactor pressure vessel (RPV) steels and the associated primary pressure boundary system. In routine RPV surveillance programs to measure the transition temperature shift, three-point bend testing of precracked Charpy-type (PCVN) specimens becomes necessary in macroscopic measurements of cleavage fracture toughness (J_c, or the corresponding K_{Jc}-value) due to severe limitations on material availability. Similarly, a number of recent applications also involve the use of small-scale fracture specimens to measure fracture toughness properties when limited material availability and test machine capacity are of major concern. These applications include, for example, fracture toughness measurements of specific microstructures in the heat affected zone of girth welds for relatively thin-walled pipelines.

However, the measuring capacity of small-scale specimens for fracture toughness prior to constraint loss may be insufficient for moderate strength pressure vessel and structural steels. Here, extensive plastic deformation precedes unstable cleavage fracture. In such conditions, the evolving crack-tip plastic zones developing from the free surfaces affect strongly the levels of near-tip stress triaxiality (constraint) with increased loading. Such constraint variations ahead of crack tip most often produce significant elevations in the measured elastic-plastic fracture toughness for these small-scale configurations tested in the low-to-mid range of the DBT region. Moreover, these changes in the crack-tip stress fields, over a relatively small thickness, coupled with a smaller sampling volume for cleavage fracture underlie an absolute thickness effect on measured toughness values, including their statistical scatter and average value (either the mean and the median values). There is clearly a synergistic effect of constraint loss and random variations of microfeatures along the crack front, including microstructural flaws, which greatly complicate the interpretation of measured fracture toughness results to define meaningful values which can effectively provide accurate assessments of structural integrity and material degradation. For example, a recently developed procedure to characterize fracture toughness data over the DBT region, often known as the Master Curve approach [6–9] and standardized in the form of ASTM E1921 [3], makes extensive use in practice of PCVN specimens to determine a reference temperature, T_0, and the associated median fracture toughness applicable to a wide range of structural ferritic steels. While some studies [10,11] suggest that use of subsize fracture specimens, including the PCVN configuration, provides acceptable, albeit slightly nonconservative, estimates of T_0, others (see, for example, [12]) indicate rather large differences in T_0-values estimated from PCVN specimens when compared to T_0-values measured using larger specimens. Currently, the issue of crack front constraint and its implications on small specimen toughness values continue to raise concerns in defect assessment and regulatory procedures.

Much recent research has focused on the utilization of alternative specimen geometries in fracture toughness measurements for specific applications including, for example, flaw acceptance criteria for surface cracks that form during fabrication or during in-service operation of pipeline girth welds. Testing of these specimen configurations has evolved primarily along the development of low constraint specimens (see [13–18] for representative experimental studies) containing shallow cracks or subjected to predominantly tensile loading to measure less conservative, higher apparent fracture toughness values. In this work, however, we explore another line of investigation in which a different bend specimen design is utilized to produce increased levels of crack-tip constraint (relative to the standard three-point bend specimen) which may be expected to alleviate some of the toughness measurement issues associated with the PCVN specimen just observed. Among the various types of crack-notch specimens used in fracture toughness testing of structural materials and metallic alloys, the single edge-notched geometry loaded in three-point bending was one of the earliest fracture toughness test specimens [19]. In retrospect, the standard single edge-notched, three-point (3P) bend specimen having a span, S, over width, W, ratio of $S/W = 4$ was introduced at the 1966 meeting of ASTM Committee E-24 on Fracture Testing of Metals [20] as one of the recommended geometries for plane strain fracture toughness measurements. The 3P bend geometry undoubtedly represents since then one of the most common specimen configurations currently adopted by several standardized test procedures, including ASTM E1820 [2], ASTM E1921 [3], ISO 12135 [21] and ISO 15653 [22], among others. While the ratio $S/W = 4$ was chosen to minimize specimen dimensions as much as possible, thereby making most effective use of available test material and testing machine loading capacity, the specimen span can advantageously be increased (while keeping other dimensions fixed) to alter its measuring capacity. Specifically in the case of small specimens, including the PCVN geometry, this approach may bring cleavage fracture toughness data from different specimen configurations into better correspondence as required by the Master Curve methodology.

Motivated by these observations, this work addresses the development of a fracture toughness test procedure using standard and non-standard SE(B) specimens, including non-standard 4-point bend configurations, and applications to investigate the cleavage fracture behavior of a high strength, low alloy structural steel. Our presentation will be given in two parts. In the present study, extensive plane-strain finite element analyses are conducted on non-standard bend geometries with varying specimen span over width ratio (S/W) and loaded under 3-point and 4-point bending. First, we characterize the potential influence of specimen geometry and loading on fracture behavior in terms of $J-Q$ descriptions to quantify constraint effects. Next, we provide a large new set of plastic η-factors applicable to these non-standard bend geometries which serve to estimate the experimentally measured toughness values in terms of load-displacement records, including the J-integral and the crack tip opening displacement (CTOD). To facilitate contact with other test protocols, such as BS 7448 [23] and ISO 12135 [21], a new set of rotational factors, r_p, to determine the CTOD based on the plastic hinge model is also provided. The extensive numerical analyses conducted here provide a large set of fracture toughness test parameters, which not only validate the existing relationships available in current standards, but also provide support to standardization efforts for fracture toughness testing using non-standard bend geometries. Fracture toughness testing conducted on

various non-standard bend specimen geometries made of a low alloy A572 Grade 50 steel plate to measure the cleavage fracture resistance data in terms of the J-integral at cleavage instability, J_c, and an exploratory application to determine the reference temperature, T_0, derived from the Master Curve methodology are considered in Part II of this study.

2. Estimation procedure of experimental fracture toughness

This section provides the essential features of the analytical framework needed to determine J and CTOD for the non-standard fracture bend specimens based upon experimental measurements of load-displacement records. We begin by considering the estimation procedure for J derived from the plastic area under the load-displacement curve and then take up the CTOD evaluation method. The presentation begins with the J-integral analysis for a cracked body based upon the plastic work measured from load-displacement records in terms of crack mouth opening displacement (CMOD or V) and load-load line displacement (LLD or Δ). Subsequent development focuses on a related procedure to evaluate CTOD from J. The description that follows also includes a CTOD evaluation scheme using a plastic hinge model.

2.1. J-integral based on plastic area

The experimental investigation of specimen geometry and loading mode effects on cleavage fracture toughness values described in Part II covers fracture tests performed on standard and non-standard bend specimens. Since the experimental evaluation of J_c-values represents a key step in the testing program to determine the reference temperature, T_0, we briefly comment on the test method aspects that have a direct bearing on the measured cleavage toughness data. Readers are referred to Ruggieri and co-workers [24–26] for a more complete discussion.

Evaluation of the J-integral from laboratory measurements of load-displacement records is most often accomplished by considering the elastic and plastic contributions to the strain energy for a cracked body under Mode I deformation [27] as follows

$$J = J_e + J_p \tag{1}$$

where the elastic component, J_e, is given by

$$J_e = \frac{K_I^2}{E'} \tag{2}$$

in which $E' = E$ or $E' = E/(1-\nu^2)$ whether plane stress or plane strain conditions are assumed with E and ν representing the (longitudinal) elastic modulus and Poisson's ratio. In the above, K_I is the (Mode I) elastic stress intensity factor for a 3P SE(B) specimen given by [27], Tada et al. [28] and ASTM E1820 [2]. The Appendix provides an improved solution to determine parameter K_I for a 4P bend specimen.

The plastic component, J_p, is conveniently evaluated from the plastic area under the load-displacement curve as

$$J_p = \frac{\eta_J A_p}{B_N (W-a_0)} \tag{3}$$

where a_0 is the original crack size (fatigue precrack notch size), B_N defines the net specimen thickness at the side groove roots ($B_N = B$ if the specimen has no side grooves where B is the specimen gross thickness), W is the width of the cracked configuration, A_p represents the plastic area under the load-displacement curve and factor η_J is a nondimensional parameter which describes the effect of plastic strain energy on the applied J. The previous definition for J derives from the assumption of nonlinear elastic material

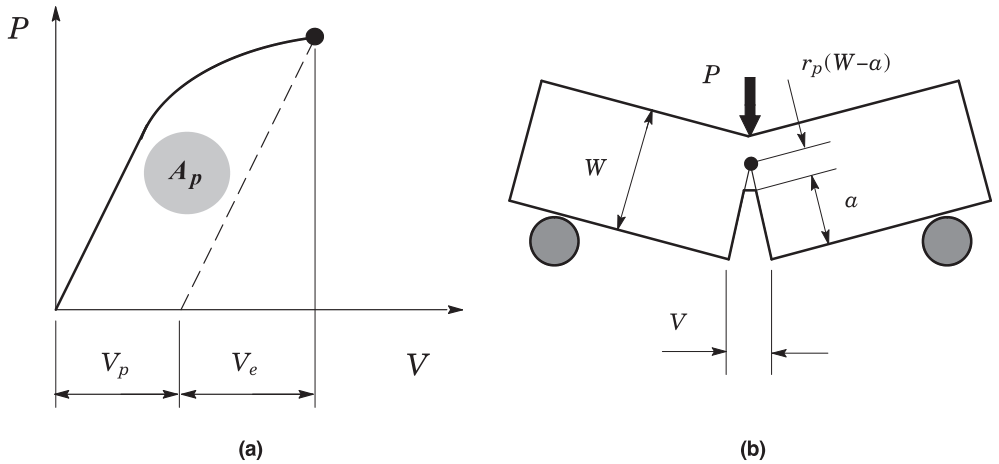

Fig. 1. (a) Schematic illustration of the evaluation procedure for the J-integral based on load-displacement records. (b) Specimen rotation for a bend loading and location of the hinge point along the crack ligament assuming straight crack profile.

response thereby providing a deformation plasticity quantity. Fig. 1(a) illustrates the procedure to determine the plastic area to calculate J from a typical load-CMOD (V) curve. While A_p (and consequently η_J) can be defined in terms of load-load line displacement (LLD) data, current testing protocols to measure fracture toughness values employing bend specimens favor the use of load-crack mouth opening displacement (CMOD) data; here, this quantity is denoted η_J^{CMOD}. However, factor η_J corresponding to LLD, here denoted η_J^{LLD}, may be required when, for example, conducting a crack growth resistance test using bend specimens to correct J for crack growth [29]. Section 5.2 provides wide range η_J-factor solutions for standard and non-standard bend specimens based on CMOD and LLD data.

2.2. Crack tip opening displacement

2.2.1. CTOD derived from plastic area: J-CTOD relationship

The previous framework also applies when the CTOD is adopted to characterize the crack-tip driving force. Under conditions of large-scale yielding, a strong relationship between J and CTOD holds along a wide range of applied loading such that the connection between J and the crack-tip opening displacement (δ) under large scale yielding [30,31] can be approximated by

$$\delta = \frac{J}{m\sigma_f} \tag{4}$$

in which m is a proportionality coefficient and σ_f represents the flow stress defined by $\sigma_f = (\sigma_{uts} + \sigma_{ys})/2$, in which σ_{ys} is the yield stress and σ_{uts} denotes the tensile strength, to incorporate the effects of strain hardening on the J *vs* CTOD relation. Here, we note that parameter m relates to total value of J to the total value of CTOD and is strongly dependent on strain hardening [30,2]. The above expression has also been adopted earlier by Kirk and Dodds [30] and Kirk and Wang [32] to develop improved CTOD estimation formulas for standard 3P bend fracture specimens. Section 5.3 addresses the J-CTOD relationships for the non-standard bend specimens considered in the present work and provides a set of m-parameters applicable to determine the CTOD from J for 3P and 4P bend geometries with varying crack sizes and S/W-ratios.

2.2.2. The plastic hinge model

Current standards to estimate the crack tip opening displacement from measured load-CMOD records for homogeneous fracture specimens, such as BS 7448 [23], also evaluate the CTOD parameter in terms of its elastic, δ_e, and plastic, δ_p, components yielding

$$\delta = \delta_e + \delta_p = \frac{K_I^2}{2\sigma_{ys}E'} + \frac{r_p(W-a_0)V_p}{r_p(W-a_0) + a_0 + z} \tag{5}$$

in which V_p represents the plastic component of the CMOD (V), z is the knife edge height ($z = 0$ if the clip gage is attached directly in the specimen) and r_p is the plastic rotational factor which defines the relative position of the (apparent) hinge point on the crack ligament [27].

Within this methodology, the plastic component of CTOD is derived from considering that the test specimen rotates about a plastic hinge located in the crack ligament as illustrated schematically in Fig. 1(b). Since the approach relies on the assumption of a rigid specimen rotation about a hinge point, it can be extended in a straightforward manner to 3P bend geometries with increased span as well as 4P bend configurations. Section 5.4 provides an extensive set of r_p for standard and non-standard bend specimens with varying crack sizes and different material properties.

3. Description of crack-front constraint: the $J-Q$ approach

The assessment of specimen geometry and loading mode (bending *vs.* tension) effects on fracture behavior for structural steels in the ductile-to-brittle (DBT) transition has received considerable attention in recent years. At increased loads in a finite body, such as a cracked specimen or structure, the initially strong high constraint fields under well-contained plasticity gradually change to fields under large scale yielding (LSY) as crack-tip plastic zones increasingly merge with the global bending yielding on the nearby traction free boundaries. This phenomenon, often termed loss of constraint, contributes to the apparent increased toughness observed in fracture testing of shallow cracked and tension loaded geometries [33,34]. While a number of approaches have been proposed to describe effects of constraint changes on fracture behavior, the present work focuses on a widely adopted methodology to quantify the evolving level of stress triaxiality ahead of the crack front under increased remote loading based upon the $J-Q$ framework. This section introduces the essential features of the methodology needed to assess effects on crack front stress triaxiality in the analyzed fracture specimens.

Development of a two-parameter characterization of the elastic-plastic crack-tip fields begins by considering a cracked body subjected to a remote stress in which crack-tip deformation scales with J/σ_0 where J denotes Rice's J-integral [35] and σ_0 is a reference (yield) stress. At load levels sufficiently small so that crack-tip plasticity is limited, it can be shown that the mode I plane-strain elastic-plastic near-tip fields can be described by a single family of crack-tip fields with varying stress triaxiality. These arguments motivated O'Dowd and Shih (OS) [36,37] to propose an approximate two-parameter description for the elastic-plastic crack tip fields based upon a triaxiality parameter more applicable under large scale yielding (LSY) conditions for materials with elastic-plastic response described by a power hardening law given by $\epsilon/\epsilon_0 \propto (\sigma/\sigma_0)^n$. Here, n denotes the strain hardening exponent, σ_0 and ϵ_0 are the reference (yield) stress and strain, respectively. Guided by detailed numerical analyses employing a modified boundary layer

(MBL) model, originally proposed by Rice [38], OS [36,37] identified a family of self-similar fields in the form

$$\sigma_{ij} = \sigma_0 f_{ij}\left(\frac{r}{J/\sigma_0}, \theta, Q\right) \tag{6}$$

where the dimensionless second parameter Q defines the amount by which σ_{ij} in fracture specimens differ from the adopted reference SSY solution with the T-stress term [39–42] set to zero. In the above Eq. (6), r and θ are polar coordinates centered at the crack tip with $\theta = 0$ corresponding to a line ahead of the crack.

Limiting attention to the forward sector ahead of the crack tip between the SSY and the fracture specimen fields, OS showed that $Q\sigma_0$ corresponds effectively to a spatially uniform hydrostatic stress, i.e., the difference field relative to a high triaxiality reference stress state

$$(\sigma_{ij})_{FB} = (\sigma_{ij})_{SSY} + Q\sigma_0\delta_{ij} \tag{7}$$

where the dimensionless second parameter Q defines the amount by which σ_{ij} in fracture specimens, $(\sigma_{ij})_{FB}$, differ from the adopted high triaxiality reference SSY solution, $(\sigma_{ij})_{SSY}$. Consequently, Q is often defined as

$$Q \equiv \frac{(\sigma_{yy})_{FB} - (\sigma_{yy})_{SSY}}{\sigma_0} \tag{8}$$

where the difference field described in terms of the opening (Mode I) stresses, σ_{yy}, is conventionally evaluated at the normalized crack-tip distance $\bar{r} = r/(J/\sigma_0) = 2$, which represents a microstructurally significant distance ahead of crack tip related to the operative fracture mechanism. OS [36,37], Dodds et al. [43] and Cravero and Ruggieri [44] have also shown that Q is relatively independent of $\bar{r}$ in the range $1 \leqslant \bar{r} \leqslant 5$. Construction of $J-Q$ trajectories for structural components and fracture specimens then follows by evaluation of Eq. (8) at each stage of loading in the finite body.

4. Geometric models and finite element procedures

4.1. Standard and non-standard SE(B) specimens

Development of a fracture toughness test procedure described here covers standard and non-standard fracture test specimens loaded under 3-point (3P) and 4-point (4P) bending with different crack sizes and varying specimen span. Single edge notch bend SE(B) specimens are extensively used in fracture toughness testing of various structural materials. The prevailing geometry is the 3-point bend configuration shown in Fig. 2(a) in which S is the specimen span (distance between the roller supports). Most fracture test standards, including ASTM E1820 [2], BS 7448 [23] and ISO 12135 [21], adopt a conventional 3-point SE(B) geometry with $S = 4W$. The present study enlarges on the current test protocols to include J and CTOD estimation procedures for 3P SE(B) geometries with increased specimen span in the range $4 \leqslant S/W \leqslant 8$.

Another convenient bend test configuration, albeit not yet standardized in fracture toughness test procedures, which has gained increased interest [45–48] is the 4-point bend geometry displayed in Fig. 2(b) in which D represents the inner span. Here, the flexural bend test fixture produces a uniform moment between the two inner loading rollers in the specimen (and associated zero shear stress) as can be easily verified by using simple beam flexure theory [49,50]. To support standardization efforts for fracture toughness testing using this specimen geometry, the present analyses also cover specimen configurations in the range $4 \leqslant S/W \leqslant 8$.

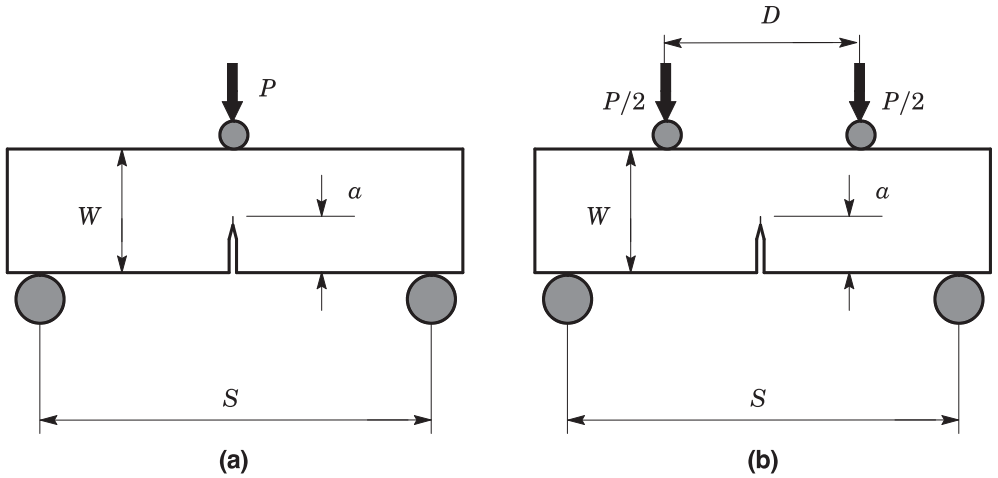

Fig. 2. Conventional bending loading geometries adopted in the present work: (a) 3-point SE(B) specimen. (b) 4-point bend specimen.

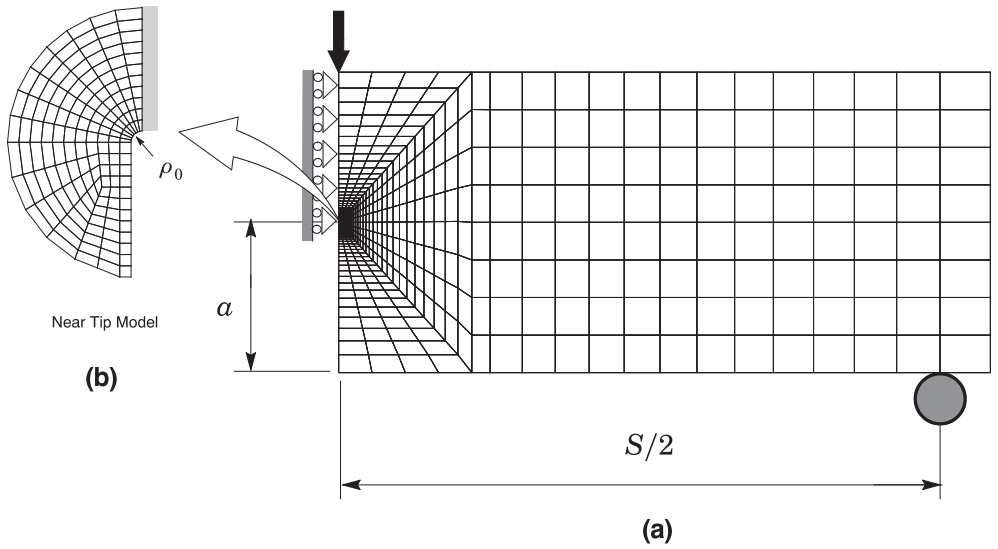

Fig. 3. Typical plane strain, finite element model for the 3-point SE(B) specimen with $a/W = 0.5$ utilized in the analyses.

4.2. Finite element models

Extensive finite element analyses are performed on plane-strain models for the 3P and 4P bend configurations described previously covering a wide range of specimen geometries and varying crack sizes. The analysis matrix builds upon a 1T reference thickness ($B = 25.4$ mm) to define a conventional specimen width of $W = 2B = 50.8$ mm for all models and includes: (1) 3-point geometries with $S/W = 4$, 6 and 8 and (2) 4-point SE(B) specimens with $S/W = 4$, 6 and 8 having a inner span $D = S/2$. The finite element models for all analyzed specimen geometries cover a range of a/W from 0.1 to 0.8 with increments of 0.1.

Fig. 3(a) shows the finite element model constructed for the plane-strain analysis of the 3P SE(B) specimen having $a/W = 0.5$. All other crack models, including the 4P bend geometry, have very similar features and are not shown here in interest of space. Special attention in terms of crack tip mesh details and very fine mesh refinement in the crack tip region was given to the finite element computations reported in the present study. We follow similar arrangement already used in our previous analyses [51,24,52,26] and adopt a conventional mesh configuration having a focused ring of elements surrounding the crack front with a small key-hole of a radius, $\rho_0 = 0.0025$ mm, at the crack tip as shown in Fig. 3(b). Symmetry conditions permit modeling of only one-half of the fracture specimens with appropriate constraints imposed on the remaining crack ligament ($u = 0$) and plane-strain constraints imposed ($w = 0$) on each node. A typical half-symmetric model has one thickness layer with $B = 1$ mm (unit thickness) and contains $\approx$ 1200–1400 8-node, 3-D elements ($\approx$ 2700–3000 nodes) for all specimen geometries. These finite element models are loaded by displacement increments imposed on the top nodes for the plane defining the applied load as shown in Fig. 3. An analogous scheme is also employed in case of the 4P bend specimen. Our previous numerical experience reveals that such displacement control loading procedure provides results which are essentially similar to those derived from loading the finite element model by a rigid roller pin using a contact procedure.

4.3. Material model and solution procedures

The elastic-plastic constitutive model employed in the numerical analyses reported here follows a flow theory with conventional Mises plasticity in small geometry change (SGC) setting representative of small strain behavior. The numerical solutions utilize a simple power-hardening model to characterize the uniaxial true stress ($\overline{\sigma}$) *vs.* logarithmic strain ($\overline{\epsilon}$) in the form

$$\frac{\overline{\epsilon}}{\epsilon_{ys}} = \frac{\overline{\sigma}}{\sigma_{ys}}, \quad \epsilon \leqslant \epsilon_{ys}\ ; \quad \frac{\overline{\epsilon}}{\epsilon_{ys}} = \left(\frac{\overline{\sigma}}{\sigma_{ys}}\right)^n, \quad \epsilon > \epsilon_{ys} \tag{9}$$

where σ_{ys} and ϵ_{ys} are the reference (yield) stress and strain, and n is the strain hardening exponent. The finite element analyses consider material flow properties covering typical structural, pressure vessel and pipeline grade steels with $E = 206$ GPa and $\nu = 0.3$: $n = 5$ and $E/\sigma_{ys} = 800$ (high hardening material), $n = 10$ and $E/\sigma_{ys} = 500$ (moderate hardening material) and $n = 20$ and $E/\sigma_{ys} = 300$ (low hardening material).

Evaluation of the J–CTOD relations described in Section 5.3 requires specification of the ultimate tensile strength, σ_{uts}, to determine the flow stress already defined previously. For each material property set, σ_{uts} is estimated using a convenient relationship between the flow properties and n as [53,54]

$$\frac{\sigma_{uts}}{\sigma_{ys}} = \left[\frac{(500/n)^{1/n}}{\exp(1/n)}\right] \tag{10}$$

which agrees well with other estimation expressions reported in the literature (see, for example, Bannister et al. [55] and API 579 [5]).

The adopted material model deserves further consideration since it is at the heart of the numerical solutions generated for the crack-tip stress fields, including the $J-Q$ trajectories, presented next. Ideally, accurate descriptions of fields near the zone of finite strains would be desirable in some applications, in which case large geometry change (LGC) analysis (which is representative of large strain behavior) is required to describe the intense strain concentration directly ahead of the crack tip. However, outside the crack-tip blunting zone, the LGC and SGC stresses converge to very similar values as demonstrated by several previous works (see, *e.g.*, Dodds et al. [56]). As will be shown later, the crack-tip stresses and parameter Q are extracted at the normalized crack-tip distance, $r/(J/\sigma_0) = 2$, which corresponds approximately to 4 × CTOD for this material [27,31]; hence, it is sufficiently far from the crack tip to avoid the strong blunting effects on the crack-tip stress fields. Consequently, the SGC analyses prove highly adequate for the present study while, at the same time, eliminating potential numerical difficulties related to convergence of the highly refined numerical models employed. It is also of interest to note that, since parameter Q quantifies the *relative* difference field between the finite cracked body and a high triaxiality reference stress state, differences between the SGC and LGC solutions remain small.

The finite element code WARP3D [57] provides the numerical solutions for the 3-D analyses reported here. These analyses employ fracture models constructed with three-dimensional, 8-node tri-linear hexahedral elements and reduced integration. Use of the so-called $\overline{\mathbf{B}}$ formulation (see [57] for details) precludes mesh lock-ups that arise as the deformation progresses into fully plastic, incompressible modes. Dilatational terms of the original strain-displacement matrix are replaced by a volume averaged set of dilatational terms which yield uniform mean stress over the element and minimal locking. To achieve plane-strain models for the current study, a single thickness layer of the 3-D elements is defined with out-of-plane displacements constrained to vanish.

The local value of the mechanical energy release rate at a point along the crack front is given by [58]

$$J = \lim_{\Gamma\to 0} \int_{\Gamma} \left[W n_1 - \sigma_{ij}\frac{\partial u_i}{\partial x_1} n_j \right] d\Gamma \tag{11}$$

where Γ denotes a contour defined in a plane normal to the front on the undeformed configuration beginning at the bottom crack face and ending on the top face, n_j is the outward normal to Γ,W denotes the stress-work density per unit of undeformed volume, σ_{ij} and u_i are Cartesian components of stress and displacement in the crack front coordinate system. The finite element computations employ a domain integral procedure [58] for numerical evaluation of Eq. (11) to provide pointwise values of J across the crack front at each loading level. These pointwise J-values are then averaged over the crack front to yield thickness average values for J retaining strong path independence for domains defined outside the highly strained material near the crack tip. Such J-values also agree very well with estimation schemes based upon η-factors for deformation plasticity [27] so that they provide a convenient parameter to characterize the average intensity of far field loading on the crack front.

The SSY reference fields required to construct the $J-Q$ trajectories addressed in Sections 5.1 are derived from plane-strain, finite element solutions of a modified boundary layer (MBL) model consisting of a (very large) circular region containing an edge crack [33,34,38,59]. With the plastic region limited to a small fraction of the domain radius, $R_p < R/20$ where R_p is the radius (size) of the crack-tip plastic zone, the general form of the asymptotic crack-tip stress fields well outside the plastic region is given by William's expansion [60] as

$$\sigma_{ij} = \frac{K_I}{\sqrt{2\pi r}} f_{ij}(\theta) \tag{12}$$

where K_I is the elastic stress intensity factor, f_{ij} define the angular variations of in-plane stress components and (r,θ) are polar coordinates centered at the crack tip. Numerical solutions for different levels of parameters $K_I = \sqrt{EJ/(1-\nu^2)}$ are generated by imposing the corresponding displacements of the elastic, Mode I singular field on the outer circular boundary ($r = R$) which encloses the crack [34].

5. Results and discussion

The following sections provide key results of the extensive numerical analyses conducted on the standard and non-standard SE(B) specimens. The presentation begins with descriptions of constraint variations characterized in terms of $J-Q$ trajectories to assess the potential effects of increased span and loading mode on fracture behavior. This is followed by the development of a new set of η-factors required to evaluate J and CTOD from measured experimental load-displacement data in fracture testing of non-standard SE(B) specimens. The section concludes with results for the plastic rotational factor, r_p, needed to evaluate the CTOD for non-standard SE(B) specimens derived from the plastic hinge model.

5.1. Effects of specimen geometry and loading mode on $J-Q$ trajectories

Figs. 4–6 display the general effects of specimen geometry, loading mode and flow properties on the $J-Q$ trajectories for the analyzed standard and non-standard bend specimens. In all plots, Q is defined by Eq. (8) at the normalized distance ahead of crack tip given by $\bar{r} = r/(J/\sigma_0) = 2$ whereas J is normalized by $(b\sigma_{ys})$ with b denoting the remaining crack ligament $(W-a)$ (notice that we plot

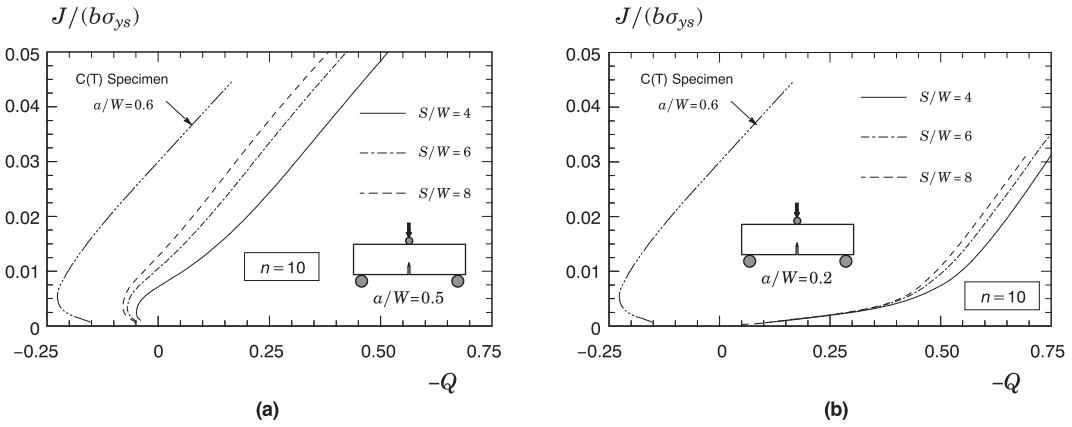

Fig. 4. $J-Q$ trajectories for 3P SE(B) specimens with varying S/W-ratios and a moderate hardening material $n = 10$ material, including the $J-Q$ trajectory for a standard C(T) specimen with $a/W = 0.6$ and same hardening material derived from Cravero and Ruggieri [44]: (a) deep crack specimen with $a/W = 0.5$; (b) shallow crack specimen with $a/W = 0.2$.

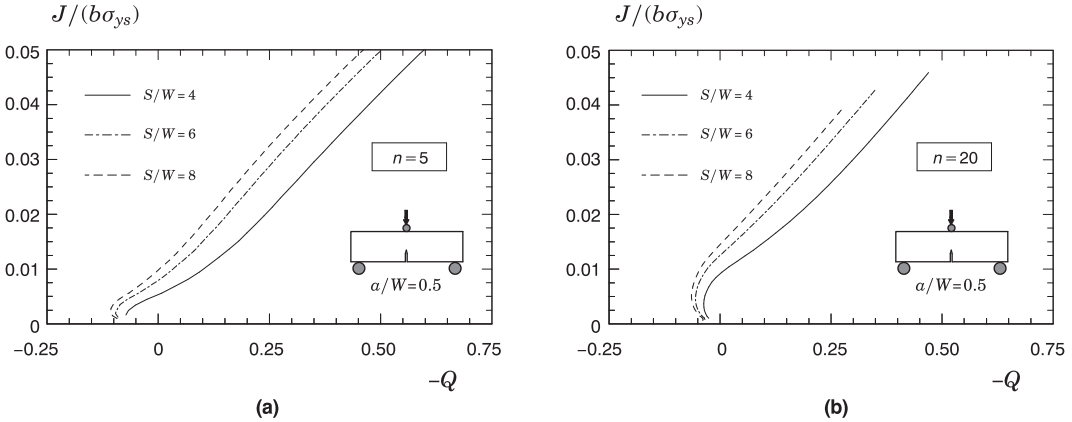

Fig. 5. $J-Q$ trajectories for deep crack, 3P SE(B) specimens with varying S/W-ratios and $a/W = 0.5$ material: (a) high hardening material with $n = 5$; (b) low hardening material with $n = 20$.

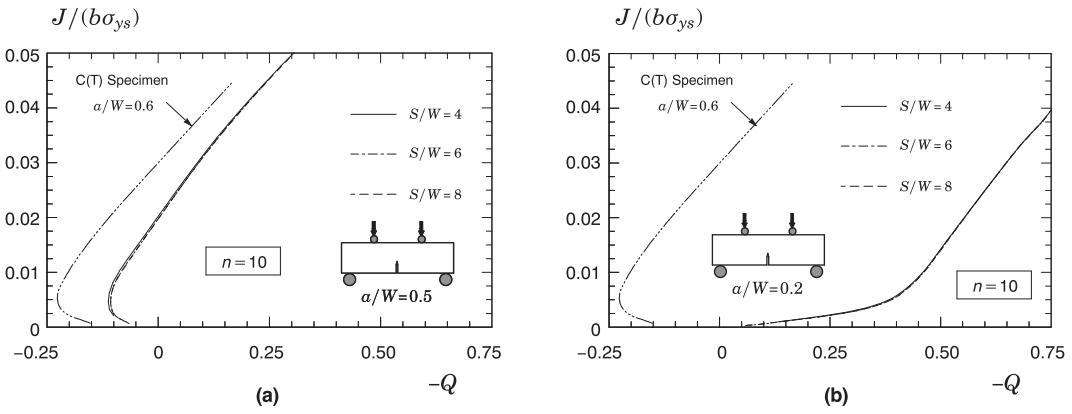

Fig. 6. $J-Q$ trajectories for 4P SE(B) specimens with varying S/W-ratios and a moderate hardening material $n = 10$ material, including the $J-Q$ trajectory for a standard C(T) specimen with $a/W = 0.6$ and same hardening material derived from Cravero and Ruggieri [44]: (a) deep crack specimen with $a/W = 0.5$; (b) shallow crack specimen with $a/W = 0.2$.

$J/(b\sigma_{ys})$ vs. $-Q$ to maintain positive scales). The material properties for all specimens were described previously in Section 4.3: $n = 5$ with $E/\sigma_{ys} = 800$; $n = 10$ with $E/\sigma_{ys} = 500$ and $n = 20$ with $E/\sigma_{ys} = 300$. The research code Fractus2D [61] is employed to compute the $J-Q$ trajectories for each fracture specimen.

Consider first Fig. 4(a) which shows the $J-Q$ curves for the deep crack, 3P SE(B) specimen with increased S/W-ratios for the

$n = 10$ material. To aid in assessing the effect of increased span on the evolution of Q with J for the SE(B) specimens, the plot also includes the $J-Q$ trajectory for a deeply-cracked, standard C(T) specimen with $a/W = 0.6$ and same hardening material derived from Cravero and Ruggieri [44]. The trend is clear. Crack-tip constraint, here characterized by parameter Q, is increased with increased specimen span as the $J-Q$ curves shift entirely to the left. Consider now the $J-Q$ curves for the shallow crack, 3P SE(B) specimen with increased S/W-ratios for the $n = 10$ material shown in Fig. 4(b). Here, an increased specimen span appears to play a lesser role for this specimen configuration as the $J-Q$ trajectories are somewhat less sensitive to the S/W-ratio. Fig. 5 displays the effect of S/W-ratio on the evolution of Q with J for the deeply-cracked SE(B) specimen under 3P loading for the high hardening ($n = 5$) and ($n = 20$) materials. Not surprisingly, the general trends remain as crack-tip constraint is also increased with increased specimen span for any flow properties considered.

Fig. 6 compares the $J-Q$ trajectories for the 4P SE(B) specimen with increased S/W-ratios for the $n = 10$ material. The plots again include the $J-Q$ trajectory for a deeply-cracked, standard C(T) specimen with $a/W = 0.6$ and same hardening material derived from Cravero and Ruggieri [44]. Analyses for other hardening levels ($n = 5$ and $n = 20$) do not provide additional insight and are omitted to conserve space. These results show an interesting development in that the $J-Q$ trajectories remain virtually unchanged as the S/W-ratio increases for the deep and shallow crack specimen. Further observe that the levels of crack-tip constraint for the 4P specimen are even higher than the corresponding levels of constraint for the 3P SE(B) specimen with $S/W = 8$ - recall from previous Fig. 4 that this specimen configuration exhibits the highest crack-tip constraint for the analyzed 3P bend geometries.

The previous descriptions of crack-tip constraint for standard and non-standard geometries show a rather marked effect of specimen span on fracture behavior for the 3P bend specimen, particularly for deep crack configurations. Moreover, these results also show the influence of loading mode on increasing crack-tip constraint for the 4P bend specimen. This is suggestive of potential mitigation effects of increased span and loading mode on constraint loss often observed in fracture testing of smaller bend specimens, such as the PCVN configuration, thereby increasing their measuring capacity. While we have not investigated such behavior in more details, we argue that the constraint response for the 3P and 4P bend specimen arises from their flexural response coupled with the interaction of crack-tip plastic zones with global plastic zones. For the 3P bend specimen, relatively high shear stresses develop on the plane containing the loading point, which may further contribute to the interaction between global bending plasticity and the crack-tip fields. The 4P bend geometry, on the other hand, has constant bending moment and zero shear stresses on the plane containing the loading point thereby suggesting a smaller interaction of crack-tip plastic zones with global plastic zones and, consequently, a less pronounced constraint loss with increased plastic deformation. Moreover, it is important to keep in mind that the $J-Q$ theory applies essentially to a 2-D framework and does not reflect changes in the material sampling volume ahead of crack front as required in analysis of the coupling between in-plane and through-thickness effects on crack-front fields. Part II of this study examines effects of specimen geometry, including increased specimen span, and loading mode on experimentally measure cleavage fracture toughness for a low alloy, structural steel tested in the DBT region.

5.2. Plastic η factors

This section describes the results of the extensive plane-strain analyses performed on numerical models of standard and non-standard SE(B) specimens described previously. Evaluation of plastic η-factors for the analyzed SE(B) configurations follows from solving Eq. (3) upon computation of the plastic area, A_p, under the $P-$CMOD and $P-$LLD curves for the 3P and 4P bend geometries with varying S/W-ratios and different material properties. Before presenting the η-factors required to evaluate the J-integral from measured experimental load-displacement records, we briefly examine the numerical procedure to compute the η-values.

At each load increment, the domain integral procedure yields a thickness average J-value from which the plastic component, J_p, is evaluated. The plastic work associated with J at each load increment also follows from direct evaluation of the plastic area under the load-displacement curve. The J_p and A_p terms are normalized by simple manipulation of previous Eq. (3) to define a linear

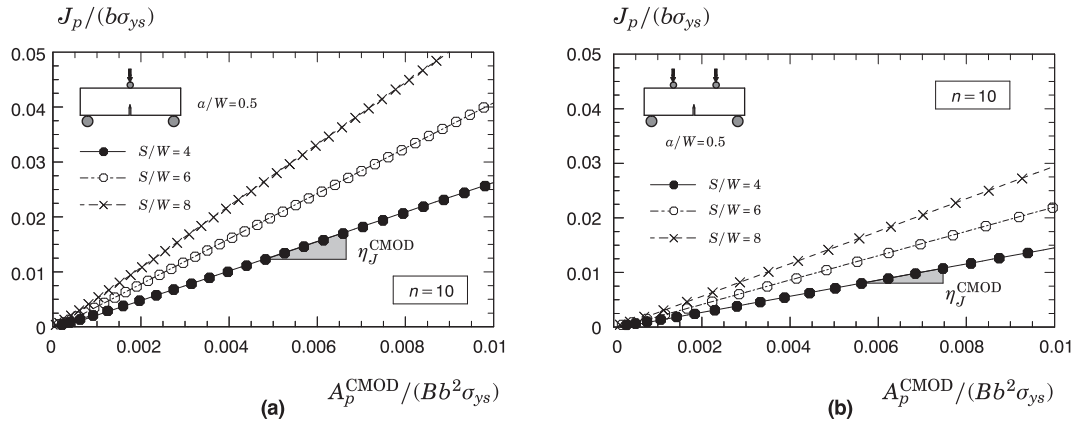

Fig. 7. Variation of normalized J_p with normalized A_p derived from CMOD records for plane-strain analyses of bend geometries with $a/W = 0.5$ and $n = 10$ material having varying S/W-ratios: (a) 3P bend specimens; (b) 4P bend specimens.

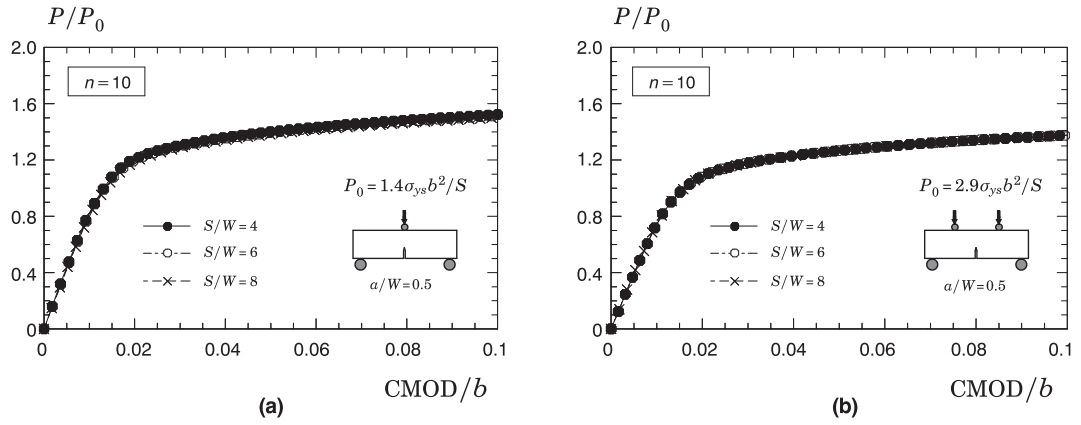

Fig. 8. Normalized load-CMOD response for the bend geometries with $a/W = 0.5$ and $n = 10$ material having varying S/W-ratios: (a) 3P bend specimens; (b) 4P bend specimens.

relationship given by $J_p/(b\sigma_{ys})$ and $A_p/(Bb^2\sigma_{ys})$ from which the plastic η-factors are evaluated. Fig. 7 shows the variation of normalized J_p with normalized A_p derived from CMOD records for the 3P and 4P bend geometries with $a/W = 0.5$ and $n = 10$ material having varying S/W-ratios. A strong linear relationship clearly holds across all configurations thereby allowing determination of factor η_J^{CMOD} by the slope of the linear regression. Such strong linear relationship displayed in Fig. 7 also holds for all other crack configurations and material properties - to conserve space, they are not shown here.

The evolution of applied load with displacement for the 3P and 4P bend configuration with different S/W-ratios is also of interest. Fig. 8 displays the load-displacement response in terms of CMOD for the 3P and 4P bend geometries with $a/W = 0.5$ and $n = 10$ material having varying S/W-ratios. In these plots, the CMOD is normalized by the crack ligament whereas the load is normalized by a convenient limit solution under plane-strain conditions for the bend specimens given by Miller [62] and expressed as

$$\frac{4M}{\sigma_{ys} W^2} = c(1-a/W)^2 \tag{13}$$

where M is the bending moment and $c = 1.398$ for the 3P bend specimen and $c = 1.456$ for the 4P bend geometry. A simple manipulation of the above expression yields the limit load, P_0, for each specimen geometry shown in Fig. 8(a-b). Because the limit load for the bend specimens depends explicitly on the specimen span, the evolution of normalized load with displacement is essentially unchanged with increased S/W-ratio indicating that the applied load simply scales with specimen span. Moreover, also observe that the load-displacement response for the 4P bend geometries lies below the corresponding response for the 3P bend specimens. Results for other SE(B) configurations and material properties do not provide additional insight and are omitted to conserve space.

Figs. 9 and 10 provide the nondimensional η-factors based on $P-$CMOD and $P-$LLD records for the 3P and 4P bend geometries with varying S/W-ratios and different material properties. In these plots, the solid symbols correspond to the computed η-values whereas the lines represent fitting curves to the numerical data. Consider first the results displayed in Fig. 9 corresponding to η-factors based on $P-$CMOD. Fig. 9(a) also includes the variation of factor η based on CMOD with a/W for the 3P bend specimen with $S/W = 4$ given by ASTM E1820 [2] for reference. The η_J^{CMOD}-values for both 3P and 4P bend geometries and every S/W-ratio considered are essentially independent of strain hardening for the entire range of a/W-ratio. Moreover, observe that the η_J^{CMOD}-value

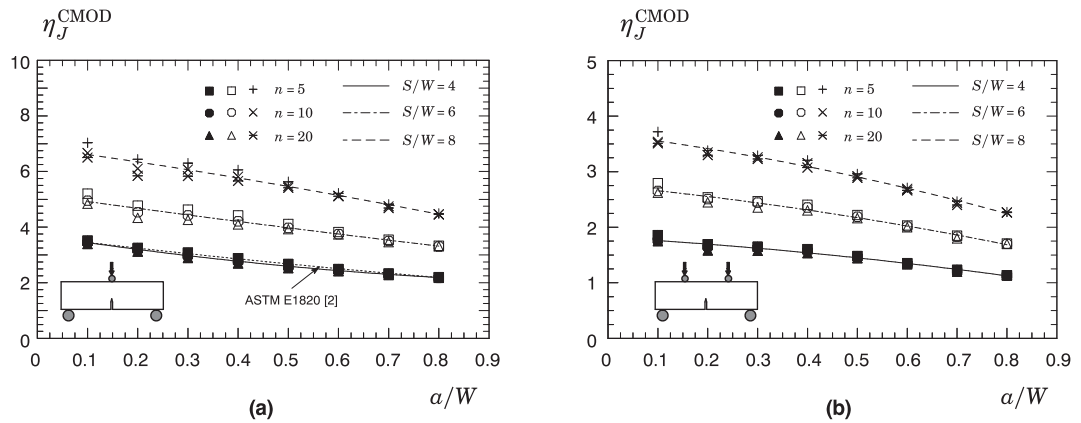

Fig. 9. Variation of plastic factor η_J with a/W-ratio derived from CMOD records for plane-strain analyses of bend geometries and varying S/W-ratios and different material properties: (a) 3P bend specimens; (b) 4P bend specimens.

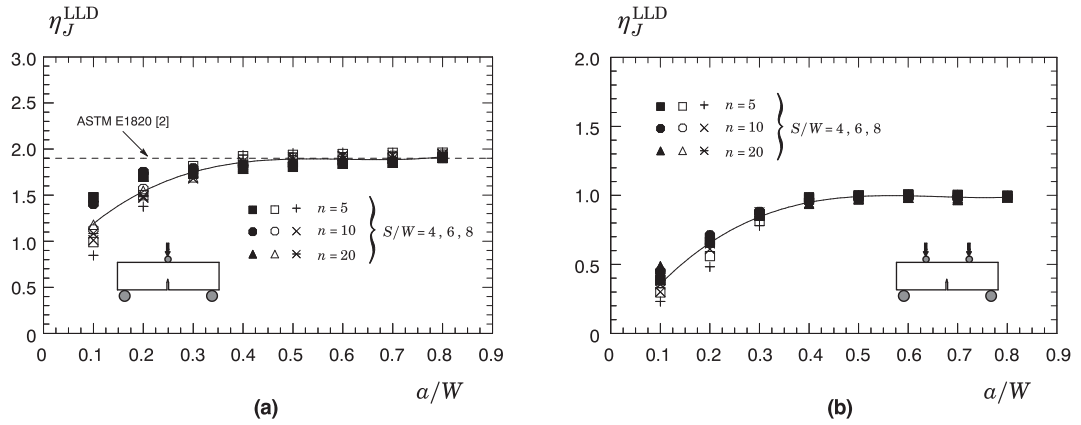

Fig. 10. Variation of plastic factor η_J with a/W-ratio derived from LLD records for plane-strain analyses of bend geometries with varying S/W-ratios and different material properties: (a) 3P bend specimens; (b) 4P bend specimens.

for a fixed a/W-ratio increases with increased S/W-ratio. Further observe that the 4P bend geometry gives rise to significantly different η_J^{CMOD}-values when compared to the η-factors for the 3P bend specimen - here, the η_J^{CMOD}-values for the 3P bend specimen are ≈ 1.8–2 higher than the corresponding values for the 4P bend geometry.

Now direct attention the results shown in Fig. 10 which describe the variation of η-factors based on P−LLD with a/W. Again, Fig. 10(a) also includes the η_J^{LLD}-value for the deeply-cracked 3P bend specimen with $S/W = 4$ given by ASTM E1820 [2] for reference. The behavior displayed by these η_J^{LLD}-values contrasts rather sharply with the previous results in that the variation of η_J^{LLD} with a/W is virtually independent of the S/W-ratio, particularly in the range $0.3 \leqslant a/W \leqslant 0.8$. The η-factors exhibit a somewhat larger sensitivity to the S/W-ratio in the case of shallow cracks ($a/W \leqslant 0.2$) but which are nevertheless reasonably close to each other, indicating a high degree of similarity for practical applications in fracture test procedures. Similarly to the previous results, the η_J^{LLD}-values for the 3P bend specimen are ≈ 1.9–2.5 higher than the corresponding values for the 4P bend geometry.

To provide a simpler manipulation of the previous results and using the plots displayed in Figs. 9 and 10 for guidance, a functional dependence of nondimensional η-factors for the 3P and 4P bend geometries with crack size is constructed in the form

$$\eta_J^{CMOD} = \alpha_0 + \alpha_1(a/W) + \alpha_2(a/W)^2 \tag{14}$$

and

$$\eta_J^{LLD} = \beta_0 + \beta_1(a/W) + \beta_2(a/W)^2 + \beta_3(a/W)^3 \tag{15}$$

where it is understood that a 2-nd order and 3-rd polynomial fittings are employed to describe the variation of factors η_J^{CMOD} and η_J^{LLD} in the range $0.1 \leqslant a/W \leqslant 0.8$ for any hardening exponent. In this regard, it deserves mention that, although it is evident from Fig. 10 that factor η_J^{LLD} shows some sensitivity to the hardening behavior for shallow cracks, the adopted polynomial fitting should be accurate enough for most practical applications which generally involve fracture testing of moderate-to-deep cracks ($a/W \geqslant 0.25$–0.3). Moreover, we also note that, while there is an almost linear relationship between η_J^{CMOD} and a/W displayed in Fig. 9, we follow similar procedure given by ASTM E1820 [2] and adopt a 2-nd order polynomial fitting to describe the variation of factor η_J^{CMOD} with crack size. Tables 1 and 2 provide the polynomial coefficients of Eqs. (14) and (15) derived from a standard least square fitting.

5.3. J-CTOD relationships

This section describes the results of the extensive plane-strain analyses performed on models for the non-standard SE(B) specimens described previously. Before addressing the functional dependence of parameter $m = J/(\delta\sigma_f)$ for the specimen geometries under discussion, we briefly examine the variation of CTOD with increased values of the J-integral, which has a direct bearing on accurate evaluation of meaningful m-values that are independent of loading. Fig. 11 provides the evolution of CTOD with J for the 3P and 4P

Table 1
Coefficients for the polynomial fitting of Eq. (14) defining the relationship between η_J^{CMOD} and a/W for the 3P and 4P bend geometries.

Specimen	Geometry	α_0	α_1	α_2
3-Point SE(B)	$S/W = 4$	3.7096	−2.7822	1.0953
	$S/W = 6$	5.1664	−2.5011	0.2350
	$S/W = 8$	6.8647	−2.4769	−0.6622
4-Point SE(B)	$S/W = 4$	1.8165	−0.5182	−0.4340
	$S/W = 6$	2.7494	−0.8673	−0.5779
	$S/W = 8$	3.6733	−1.1219	−0.8308

Table 2
Coefficients for the polynomial fitting of Eq. (15) defining the relationship between η_J^{LLD} and a/W for the 3P and 4P bend geometries.

Specimen	Geometry	β_0	β_1	β_2	β_3
3-Point SE(B)	All S/W	5.6942	−10.3550	6.1979	0.6689
4-Point SE(B)	All S/W	−0.0705	5.0186	−7.7424	3.9104

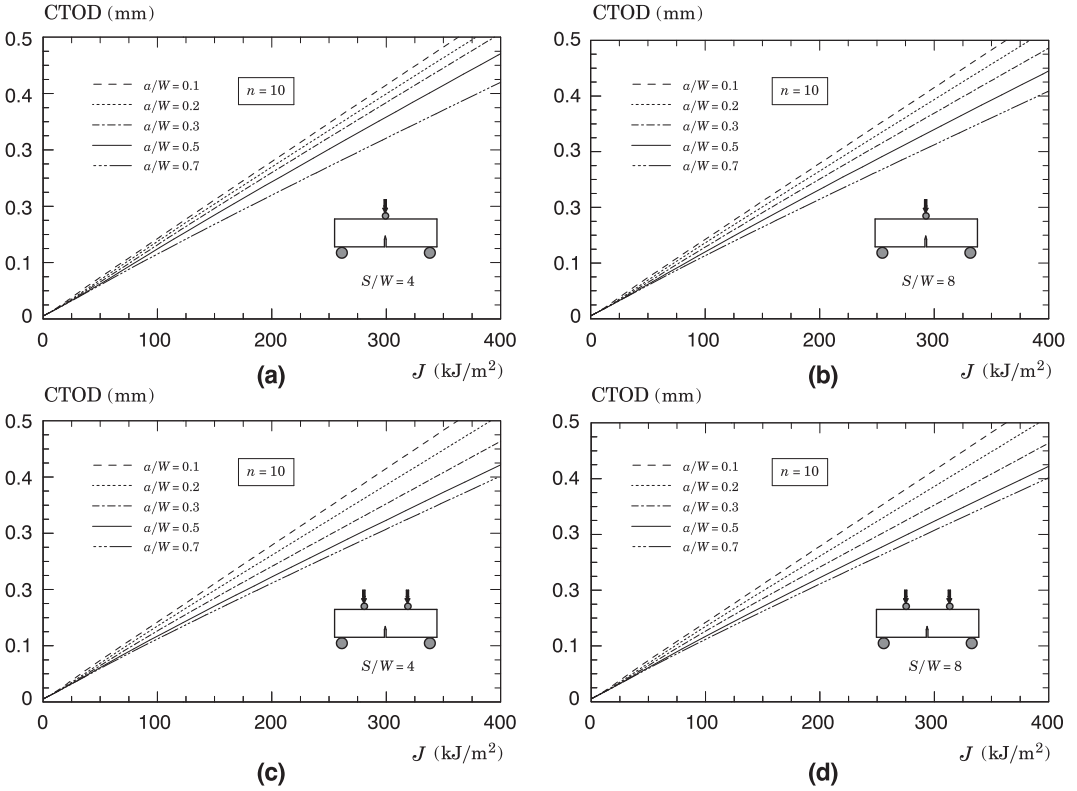

Fig. 11. J-CTOD relation for the SE(B) geometries with varying a/W-ratio and $n = 10$ material; (a) 3P specimen with $S/W = 4$; (b) 3P specimen with $S/W = 8$; (c) 4P specimen with $S/W = 4$ (d) 4P specimen with $S/W = 8$.

SE(B) specimens with varying S/W-ratio and selected a/W-ratios for the moderate strain hardening material ($n = 10$). Observe that, apart from small differences, the J-CTOD relations are relatively independent of the S/W-ratio for a fixed loading mode and that the evolution of CTOD with increased J follows a fairly straight line for almost the entire range of loading. Further observe that the 4P bend geometry gives rise to J-CTOD relations which do not differ significantly from the corresponding relationships for the 3P bend specimen. The trends and results described here are essentially similar for other strain hardening materials and S/W-ratio but are not shown here in interest of space.

Fig. 12 shows the evolution of parameter m with increased loading, as characterized by increased values of J, for the 3P and 4P SE(B) geometries with varying S/W-ratio and selected a/W-ratios for the moderate strain hardening material ($n = 10$). For reference, the plane-strain m-value corresponding to a standard bend specimen with $S/W = 4$ and $a/W = 0.5$ derived from ASTM E1820 [2] is also included in the plot of Fig. 12(a). The m-values display strong variation at small levels of loading (which are associated with small J-values) for every case under consideration; such behavior derives directly from a strong nonlinear relationship between J and CTOD early in the loading of the specimen. After this transitional behavior, the m-values increase slowly with increased J and attain an essentially constant value for each of the a/W-ratios considered. Here, it can be easily seen that, apart from the very deep crack specimen with $a/W = 0.7$, the loading level at which the m-values reach a "plateau" is conservatively given by $J \approx 200$ kJ/m^2. For the $n = 10$ material and specimen geometry with $S/W = 4$, these plateau values range from $m \approx 1.9$ for $a/W = 0.7$ to $m \approx 1.5$ for $a/W = 0.1$.

The above results, including others derived from additional analyses conducted on plane-strain models for different specimen geometries and material properties to construct the J-CTOD relations, are used to determine the variation of parameter m with crack size for the 3P and 4P SE(B) specimen displayed in Fig. 13. The results shown in these plots provide support to the following observations: (1) The m-values for the 3P and 4P geometries are essentially independent of specimen span, as characterized by the S/W-ratio; (2) The m-values display more sensitivity to the strain hardening exponent in the range $5 \leqslant n \leqslant 10$ for both bend

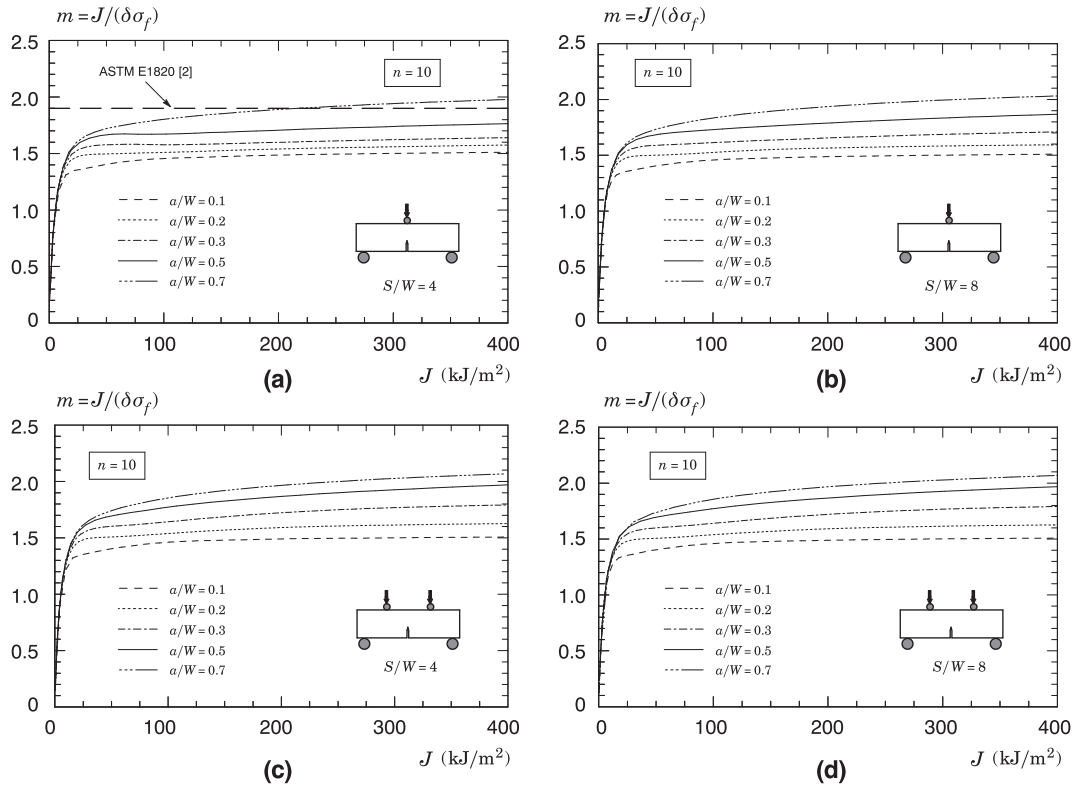

Fig. 12. Evolution of parameter m with increased load level for the bend specimens with varying a/W-ratio and $n = 10$ material.

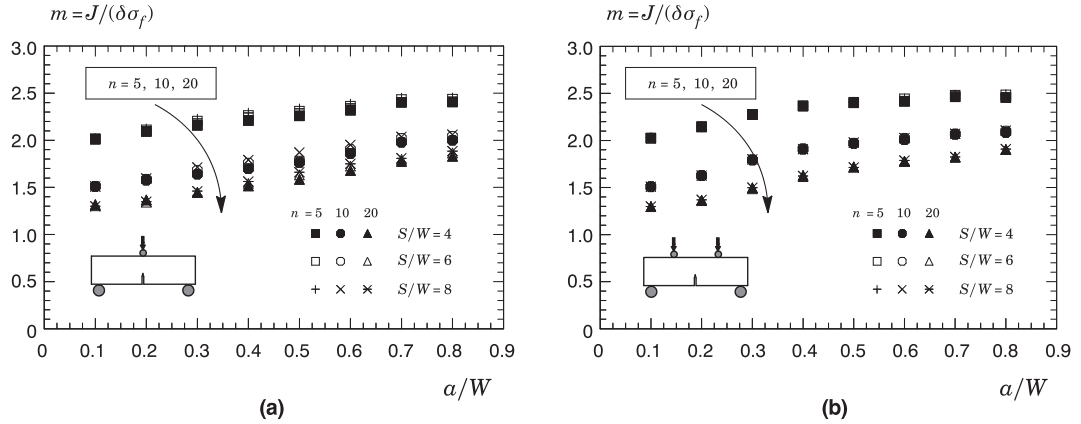

Fig. 13. Variation of parameter m with crack size for the bend specimens with different geometries and material properties.

geometries; (3) The m-values show similar trends irrespective of loading mode considered (3P *vs.* 4P).

To provide a simpler manipulation of the previous results displayed in Fig. 13, a functional dependence of parameter m with crack size, a/W, and hardening exponent, n, for the bend geometries is obtained in the form

$$m_{3P} = 0.8603 + 0.9068(a/W) - 0.1814(a/W)^2 + 5.1027n^{-1} + 0.0052n \tag{16}$$

and

$$m_{4P} = 0.9781 + 1.6154(a/W) - 0.9092(a/W)^2 + 4.3640n^{-1} - 0.0035n \tag{17}$$

where it is understood that the subscripts 3P and 4P correspond to the loading mode and a multivariate polynomial fitting [63] is adopted to describe the coupled dependence of parameter m on the a/W-ratio and n. Here, the hardening exponent can be estimated by [5]

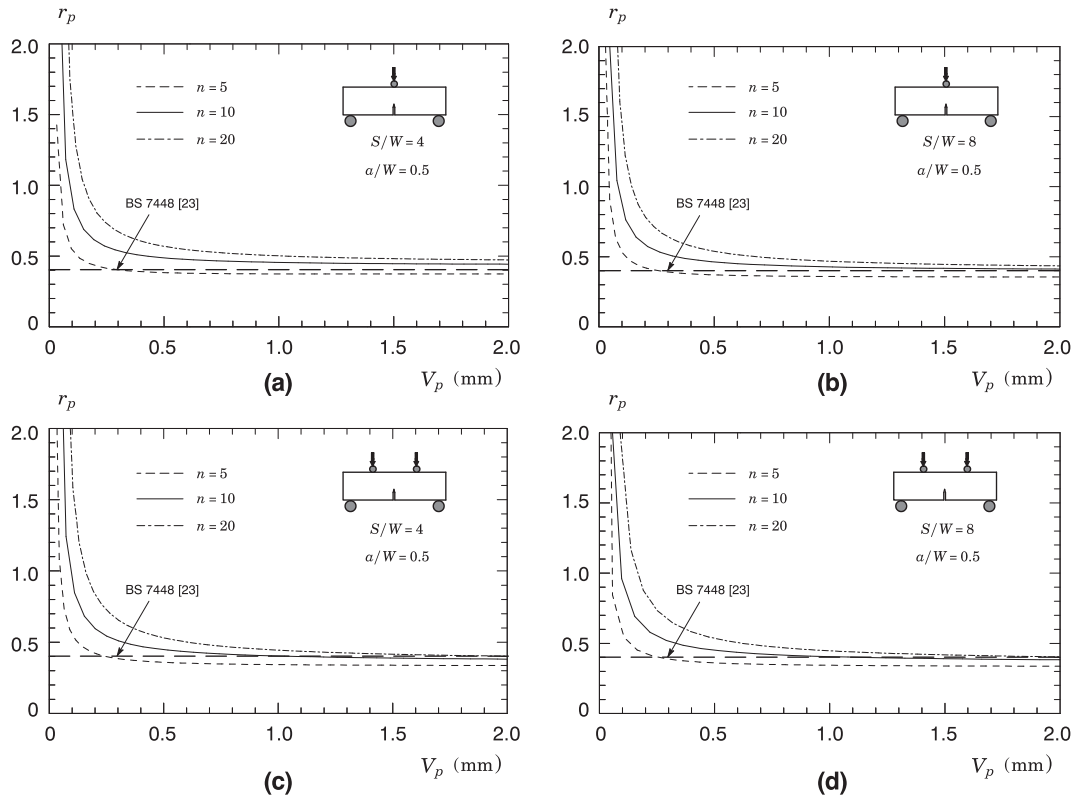

Fig. 14. Evolution of plastic rotational factor, r_p, with increased CMOD for selected 3P and 4P bend geometries with $a/W = 0.5$ and varying material properties.

$$n = \frac{1.1249 + 11.0097Y_r - 11.7464Y_r^2}{1 + 1.3495Y_r - 5.3117Y_r^2 + 2.9643Y_r^3} \tag{18}$$

in which $Y_r = \sigma_{ys}/\sigma_{uts}$. The above expressions are valid in the range $0.1 \leqslant a/W \leqslant 0.8$ and $5 \leqslant n \leqslant 20$ for any S/W-ratio. Moreover, the polynomial fitting defined by previous Eqs. (16) and (17) gives results in excellent agreement with the computed m-values displayed in Fig. 13 in which differences between the fitted and numerical values are less than 5%.

5.4. Plastic rotational factors

The procedure to estimate the CTOD outlined in Section 2.2.2 relies on the assumption of a rigid specimen rotation about a hinge point to evaluate the plastic component, δ_p, from the measured crack mouth opening displacement. Here, we provide the r_p-values derived from detailed plane-strain analyses of the standard and non-standard SE(B) specimens with a wide range of crack sizes and material properties.

Following similar previous developments, we first consider the variation of r_p with increased specimen deformation as measured by the CMOD for selected specimen geometries with different material properties. The plastic rotational factor for each analyzed SE(B) specimen configuration is derived from evaluation of δ_p in Eq. (5) and then solving for r_p. Fig. 14 shows the variation of the plastic rotational factor with the plastic component of CMOD, V_p, for the deeply cracked SE(B) specimen with $a/W = 0.5$ under 3P and 4P bend loading having $S/W = 4$ and 8 with different flow properties, $n = 5$, 10 and 20. For every case considered in Fig. 14, the r_p-values varies strongly for low values of V_p for which the plastic hinge model is highly inaccurate as elastic and plastic displacements have similar order of magnitude. In contrast, with increased values of V_p, factor r_p does reach a fairly constant value essentially independent of V_p. In particular, r_p approaches the value of 0.4 given by BS 7448 [23] for a standard SE(B) geometry with $a/W = 0.5$ and $S/W = 4$ as indicated in the plots. Indeed, these results show that the evolution of r_p with V_p exhibits almost not sensitivity to specimen span and loading mode (3P *vs.* 4P) The response displayed in these plots enables an interesting interpretation with important implications in that the r_p-value specified by BS 7448 [23] may serve equally well to determine the CTOD from measured load-CMOD records for deeply cracked SE(B) specimens under either 3P or 4P bend loading and with any S/W-ratio in the range $4 \leqslant S/W \leqslant 8$.

Fig. 15 provides the variation of factor r_p with increased a/W-ratio for the 3P and 4P bend geometries having $S/W = 4$ and 8 with different flow properties, $n = 5$, 10 and 20. As already introduced in the previous figure, these r_p-factors represent the constant values which develop in the r_p *vs.* V_p plot for each specimen configuration and hardening property (see Fig. 14). For deeply cracked bend

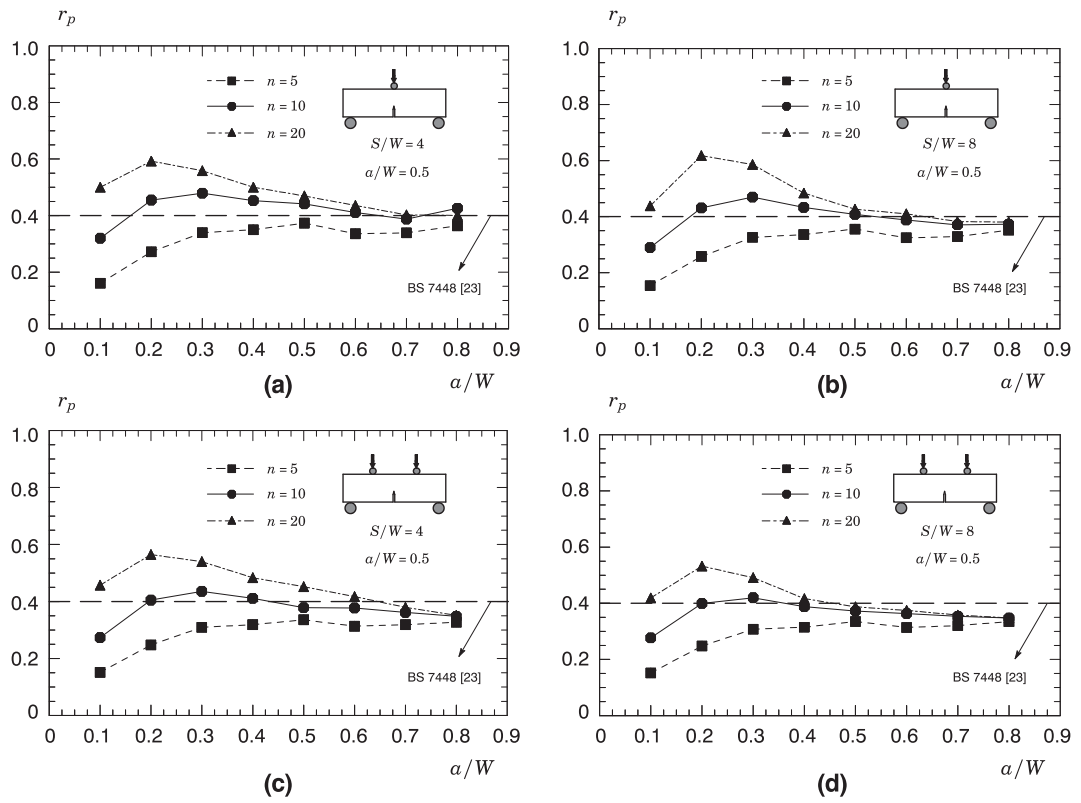

Fig. 15. Variation of plastic rotational factor, r_p, with a/W-ratio for selected 3P and 4P bend geometries with varying material properties.

specimens ($a/W \gtrsim 0.45$–0.5), the r_p -values can be assumed relatively independent of crack size and hardening properties. Such behavior contrasts sharply with the variation of r_p with a/W-ratio for shallow cracks as factor r_p now depends strongly on crack size and strain hardening behavior. Moreover, for a given bend loading mode (3P and 4P), the variation of factor r_p with increased a/W-ratio depends rather weakly on specimen span as characterized by the S/W-ratio.

To facilitate manipulation of the previous results to estimate the CTOD from measured records of crack mouth opening displacement based on the plastic hinge model, a functional dependence of factor r_p with crack size, a/W, and hardening exponent, n, for the bend geometries is given in the form

$$r_p = g(a/W)h(n) \tag{19}$$

where

$$g_{3P}(a/W) = -0.2951 + 3.3399(a/W) - 8.4505(a/W)^2 + 9.0285(a/W)^3 - 3.2219(a/W)^4 \tag{20}$$

$$h_{3P}(n) = 0.0492n - 0.0297n(a/W) - 0.001n^2 \tag{21}$$

and

$$g_{4P}(a/W) = -0.3085 + 3.8941(a/W) - 11.1815(a/W)^2 + 14.0742(a/W)^3 - 6.3308(a/W)^4 \tag{22}$$

$$h_{4P}(n) = 0.03813n - 0.0287n(a/W) - 0.0005n^2 \tag{23}$$

where it is again understood that the subscripts 3P and 4P correspond to the loading mode and a multivariate polynomial fitting [63] is adopted to describe the coupled dependence of factor r_p on the a/W-ratio and n. Similarly to the results described in previous section, the above polynomial fitting gives results in good agreement with the computed r_p-factor shown in Fig. 15 in which differences between the fitted and numerical values are less than 5–10%.

6. Summary and conclusions

This work describes the development of a fracture toughness test methodology to evaluate the J-integral and CTOD using standard and non-standard SE(B) specimens, including non-standard 4-point bend configurations. The analyses consider J and CTOD estimation procedures for 3-point and 4-point bend specimens based upon plastic factors and plastic rotational η-factors and include: (i) J and CTOD estimation from plastic work derived from experimentally measured load-displacement records and (ii) CTOD estimation

from the plastic hinge model using a linear relationship between the experimentally measured CMOD and CTOD. Moreover, the investigation also addresses the potential influence of specimen geometry and loading on fracture behavior in terms of $J-Q$ descriptions to quantify constraint effects. The extensive plane-strain finite element analyses conducted for 3-point and 4-point bend specimens provide a large set of plastic η-factors and r_p-values applicable to evaluate J and CTOD in non-standard bend geometries for a wide range of crack sizes (as characterized by the a/W-ratio), specimen span (as described by the S/W-ratio) and hardening properties characteristic of structural, pressure vessel and pipeline steels.

Our results reveal that specimen span and loading mode affect rather strongly the fracture behavior of bend specimens, particularly for deep crack configurations, which suggests a potential mitigation effect of increased span and loading mode on constraint loss often observed in fracture testing of smaller bend specimens, such as the PCVN configuration, thereby increasing their measuring capacity. Further, the analyses show that the η_J^{CMOD}-values for both 3P and 4P bend geometries show a rather strong dependence on the S/W-ratio but, at the same time, are essentially independent of strain hardening over a wide range of a/W-ratio for a given S/W-ratio. In contrast, the variation of η_J^{LLD} with a/W displays much less sensitivity to the S/W-ratio, particularly for moderate to deep cracks. Similarly, the analyses also show that the J-CTOD relationships for the 3P and 4P geometries are essentially independent of specimen span, as characterized by the S/W-ratio. Another result of interest emerging from our analyses is that the plastic rotational factor, r_p, exhibits almost not sensitivity to specimen span and loading mode (3P *vs.* 4P), which has important implications in that the r_p-value specified by BS 7448 [23] may serve equally well to determine the CTOD from measured load-CMOD records for deeply cracked SE(B) specimens under either 3P or 4P bend loading and with any S/W-ratio considered here. Overall, the present study broadens the applicability of current standards adopting the η-method and factor r_p in laboratory measurements of fracture toughness data using non-standard bend geometries. Part II [64] of this investigation builds upon the J evaluation procedure developed here to address an experimental investigation of the effects of geometry and loading mode on the cleavage fracture behavior of a high strength, low alloy structural steel using standard and non-standard SE(B) specimens, including a non-standard PCVN configuration.

Acknowledgments

This investigation is supported by Fundação de Amparo à Pesquisa do Estado de São Paulo (FAPESP) through research grant 2016/26024-1. The first author (VSB) would like to acknowledge the financial support from Coordenação de Aperfeiçoamento de Pessoal de Nível Superior (CAPES). The work of CR is also supported by the Brazilian Council for Scientific and Technological Development (CNPq) through grant 306193/2013-2.

Appendix A. Stress intensity factor solutions for 4-point bend specimens

Evaluation of the J-integral for the 4-point SE(B) specimens requires accurate solutions for the (Mode I) elastic stress intensity factor, K_I, to determine the elastic component of the J-integral given by Eq. (2) presented in Section 2.1. Tada et al. [28] provide the stress intensity factors for a bend geometry loaded in pure bending. The present section provides the stress intensity factor solutions for the 4-point bend specimen with varying specimen geometry (different a/W and S/W-ratios).

The stress intensity factor for a bend geometry is conveniently defined in the form [2]

$$K_I = \frac{PS}{B_N W^{3/2}} F(a/W) \tag{A.1}$$

where $F(a/W)$ defines a nondimensional stress intensity factor dependent upon specimen geometry and crack size. Here, P is the applied load, B_N denotes the net specimen thickness at the side groove roots ($B_N = B$ if the specimen has no side grooves where B is the specimen gross thickness) and W is the specimen width.

An extensive series of linear finite element analyses for the 4P bend specimens considered in the present study was conducted to evaluate the nondimensional stress intensity factor, $F(a/W)$, for different a/W and S/W-ratios. The analysis matrix (see Fig. 2) includes fracture specimens with crack sizes in the range 0.1–0.8 with increments of 0.1 and with specimen span to width ratio given by $S/W = 4$, 6 and 8. The finite element code WARP3D [57] provides the numerical solutions for the linear elastic analysis described here. For each model, evaluation of the elastic stress intensity factor follows from computational of the J-integral using the conventional relationship given by previous Eq. (2) with $\nu = 0.3$ and $E = 206$ GPa in all analyses. The finite element models employed in these computations have essentially similar mesh details as the numerical models previously described in Section 4.2.

Fig. A.1 provides the key results describing the variation of the nondimensional stress intensity factor, $F(a/W)$, with a/W-ratio for different S/W-ratios. As could be anticipated, the plot displayed in Fig. A.1 reveals that the variation of $F(a/W)$ with S/W-ratio remains unchanged for different a/W-ratios. Using these results for guidance, we construct the functional dependence of the nondimensional stress intensity factor and a/W-ratio as follows

$$F(a/W) = -0.2353 + 11.8397\frac{a}{W} - 69.7773\left(\frac{a}{W}\right)^2 + 216.0468\left(\frac{a}{W}\right)^3 - 306.6905\left(\frac{a}{W}\right)^4 + 170.5374\left(\frac{a}{W}\right)^5 \tag{A.2}$$

where it is understood that a 5-th order polynomial fitting [63] is employed. The solid lines displayed in the plot define the fitting curve corresponding to Eq. (A.2).

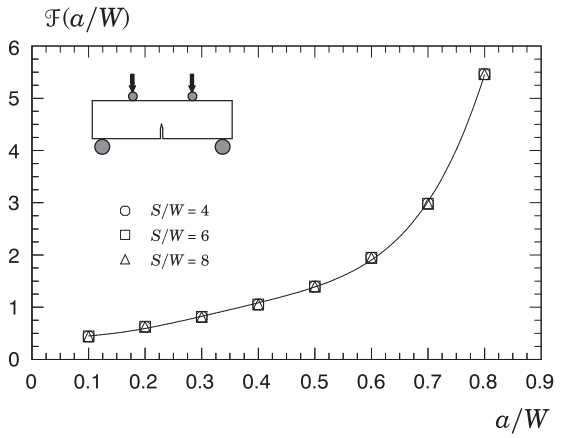

Fig. A.1. Nondimensional stress intensity factor with a/W-ratio for 4-point bend specimen with varying a/W-ratios.

References

[1] Hutchinson JW. Fundamentals of the phenomenological theory of nonlinear fracture mechanics. J Appl Mech 1983;50:1042–51.
[2] American Society for Testing and Materials. Standard test method for measurement of fracture toughness, ASTM E1820-17; 2017.
[3] American Society for Testing and Materials. Standard test method for determination of reference temperature, T_0, for ferritic steels in the transition range, ASTM E1921-17a; 2017.
[4] British Institution. Guide to methods for assessing the acceptability of flaws in metallic structures, BS 7910; 2013.
[5] American Petroleum Institute. Fitness-for-service, API RP-579-1/ ASME FFS-1; 2016.
[6] Wallin K. Fracture toughness transition curve shape for ferritic structural steels. In: Teoh SHSH, Lee KH, editors.Joint FEFG/IICF international conference on fracture of engineering materials and structures, Singapore; 1991. p. 83–8.
[7] Wallin K. Irradiation damage effects on the fracture toughness transition curve shape for reactor pressure vessel steels. Int J Press Vessel Pip 1993;55:61–79.
[8] Wallin K. Master curve analysis of the Euro fracture toughness dataset. Eng Fract Mech 2002;69:451–81.
[9] McCabe DE, Merkle JG, Wallin K. An introduction to the development and use of the master curve method. In: ASTM manual series MNL 27. ASTM International; 2005.
[10] Wallin K, Planman T, Valo M, Rintamaa R. Applicability of miniature size bend specimens to determine the master curve reference temperature T_0. Eng Fract Mech 2001;68:1256–96.
[11] Joyce JA, Tregoning RL. Development of the T_0 reference temperature from precracked charpy specimens. Eng Fract Mech 2001;68:861–94.
[12] U.S. Nuclear Regulatory Commission. Expanded materials degradation assessment (EMDA) – Volume 3: Aging of reactor pressure vessels. Tech rep. NUREG/CR-7153, vol. 3. USNRC; 2014.
[13] Joyce JA, Hackett EM, Roe C. Effects of crack depth and mode loading on the J-R curve behavior of a high strength steel. In: Underwood JH, Schwalbe K-H, Dodds RH, editors. Constraint effects in fracture, ASTM STP 1171. Philadelphia: American Society for Testing and Materials; 1993. p. 239–63.
[14] Dawes MG, Slater G, Gordon JR, McGaughy TH. Shallow crack test methods for the determination of K_{Ic}, CTOD and J fracture toughness. In: Dawes MG, editor. Shallow crack fracture mechanics toughness tests and applications. Woodhead Publishing; 1993. p. 115–25.
[15] Joyce JA, Link RE. Effects of constraint on upper shelf fracture toughness. In: Reuter WG, Underwood JH, Newman J, editors. Fracture mechanics, ASTM STP 1256. Philadelphia: American Society for Testing and Materials; 1995. p. 142–77.
[16] Scibetta M, Chaoudi R. Fracture toughness derived from small circumferentially cracked bars. In: Corwin WR, Rosinki ST, van Walle E, editors. Small specimen test techniques, ASTM STP 1329. Philadelphia: American Society for Testing and Materials; 1998. p. 363–80.
[17] Link RE. Dynamic fracture toughness measurements in the ductile-to-brittle region using small specimens. In: Reuter WG, Piascik RS, editors. Fatigue and fracture mechanics: 33rd volume, ASTM STP 1417. Philadelphia: American Society for Testing and Materials; 2002. p. 651–71.
[18] Mathias LLS, Sarzosa DFB, Ruggieri C. Effects of specimen geometry and loading mode on crack growth resistance curves of a high-strength pipeline girth weld. Int J Press Vessels Pip 2013;111–112:106–19.
[19] Srawley JE, Brown Jr. WF. Fracture toughness testing methods. Fracture toughness testing and its application, ASTM STP 381. Philadelphia: American Society for Testing and Materials; 1965. p. 133–98.
[20] Heyer RH, McCabe DE. Evaluation of a method of test for plane strain fracture toughness using a bend specimen. In: Brown WF, editor. Review of developments in plane strain fracture toughness testing, ASTM STP 463. Philadelphia: American Society for Testing and Materials; 1970. p. 22–41.
[21] International Organization for Standardization. Metallic materials – unified method of test for the determination of quasistatic fracture toughness, ISO 12135-2002; 2002.
[22] International Organization for Standardization. Metallic materials – method of test for the determination of quasistatic fracture toughness of welds, ISO 15653-2010; 2010.
[23] British Standard. Fracture mechanics toughness tests – Part 1. Method for determination ofK_{Ic}, critical CTOD and critical$J$values of metallic materials, BS 7448-1:1991; 1991.
[24] Ruggieri C. Further results in J and CTOD estimation procedures for SE(T) fracture specimens –Part I: Homogeneous materials. Eng Fract Mech 2012;79:245–65.
[25] Paredes M, Ruggieri C. Further results in J and CTOD estimation procedures for SE(T) fracture specimens – Part II: weld centerline cracks. Eng Fract Mech 2012;89:24–39.
[26] Souza RF, Ruggieri C. Revised η-factors and J-CTOD relationships for SE(B) fracture specimens including 3-D effects and implications for fracture toughness measurements. Mater Perform Charact 2015;2(2):34–54. [ASTM International].
[27] Anderson TL. Fracture mechanics: fundamentals and applications. 3rd ed. Boca Raton (FL): CRC Press; 2005.
[28] Tada H, Paris PC, Irwin GR. The stress analysis of cracks handbook. 3rd ed. American Society of Mechanical Engineers; 2000.
[29] Cravero S, Ruggieri C. Further developments in J evaluation procedure for growing cracks based on LLD and CMOD data. Int J Fract 2007;148:387–400.
[30] Kirk MT, Dodds RH. J and CTOD estimation equations for shallow cracks in single edge notch bend specimens. J Test Eval 1993;21:228–38.
[31] Shih CF. Relationship between the J-integral and the crack opening displacement for stationary and extending cracks. J Mech Phys Solids 1981;29:305–26.
[32] Kirk MT, Wang Y-Y. Wide range CTOD estimation formulae for SE(B) specimens. In: Reuter WG, Underwood JH, Newman J, editors. Fracture mechanics, ASTM STP 1256. Philadelphia: American Society for Testing and Materials; 1995. p. 126–41.
[33] Dodds RH, Shih C, Anderson T. Continuum and micro-mechanics treatment of constraint in fracture. Int J Fract 1993;64:101–33.
[34] Nevalainen M, Dodds RH. Numerical investigation of 3-D constraint effects on brittle fracture in SE(B) and C(T) specimens. Int J Fract 1995;74:131–61.

[35] Rice JR. A path independent integral and the approximate analysis of strain concentration by notches and cracks. J Appl Mech 1968;35:379–86.
[36] O'Dowd N, Shih C. Family of crack-tip fields characterized by a triaxiality parameter: Part I – Structure of fields. J Mech Phys Solids 1991;39:989–1015.
[37] O'Dowd N, Shih C. Family of crack-tip fields characterized by a triaxiality parameter: Part II – Fracture applications. J Mech Phys Solids 1992;40:939–63.
[38] Rice JR. Mechanics of crack tip deformation and extension by fatigue. In: Grosskreutz J, editor. Fatigue crack propagation, ASTM STP 415. Philadelphia: American Society for Testing and Materials; 1967. p. 247–311.
[39] Larsson SG, Carlsson AJ. Influence of non-singular stress terms and specimen geometry on small scale yielding at crack-tips in elastic-plastic materials. J Mech Phys Solids 1973;21:447–73.
[40] Betegon C, Hancock JW. Two-parameter characterization of elastic-plastic crack tip fields. J Appl Mech 1991;58:104–13.
[41] Du ZZ, Hancock JW. The effect of non-singular stresses on crack-tip constraint. J Mech Phys Solids 1991;39:555–67.
[42] Parks DM. Advances in characterization of elastic-plastic crack-tip fields. In: Argon AS, editor. Topics in fracture and fatigue. Springer-Verlag; 1992. p. 59–98.
[43] Dodds R, Anderson T, Kirk M. A framework to correlate a/W ratio effects on elastic-plastic fracture toughness (J_c). Int J Fract 1991;48:1–22.
[44] Cravero S, Ruggieri C. Correlation of fracture behavior in high pressure pipelines with axial flaws using constraint designed test specimens –Part I: Plane-strain analyses. Eng Fract Mech 2005;72:1344–60.
[45] Grabowski I, Yates JR. The effect of specimen geometry on short-crack growth behavior of a nickel-based superalloy. Int J Fatigue 1992;14(4):227–32.
[46] Yates JR, Zhang W, Miller KJ. The initiation and propagation behavior of short fatigue cracks in waspaloy subjected to bending. Fatigue Fract Eng Mater Struct 1993;16(3):351–62.
[47] Campbell JP, Ritchie RO. Mixed-mode, high-cycle fatigue-crack growth thresholds in Ti-6Al-4V – I: a comparison of large and short crack behavior. Eng Fract Mech 2000;67:209–27.
[48] Kobayashi H, Konda N, Sutep JAK, Horikawa K, Yamauchi T. Fatigue crack extension in four-point bending test for steels imitated heat affected zone. J Soc Mater Sci, Jpn 2015;64(4):323–9.
[49] Craig RR. Mechanics of materials. New York (NY): John Wiley & Sons; 1996.
[50] Gere JM. Mechanics of materials. 6th ed. Toronto (Canada): Cengage Learning; 2006.
[51] Cravero S, Ruggieri C. Estimation procedure of J-resistance curves for SE(T) fracture specimens using unloading compliance. Eng Fract Mech 2007;74:2735–57.
[52] Savioli RG, Ruggieri C. J and CTOD estimation formulas for C(T) fracture specimens including effects of weld strength overmatch. Int J Fract 2013;179:109–27.
[53] American Petroleum Institute. Fitness-for-service, API RP-579-1/ ASME FFS-1; 2007.
[54] EDF Energy Nuclear Generation Limited. Assessment of the integrity of structures containing defects, R6 Procedure Revision 4 Including Amendment 10; 2013.
[55] Bannister AC, Ocejo JR, Gutierrez-Solana F. Implications of the yield stress/ tensile stress ratio to the SINTAP failure assessment diagrams for homogeneous materials. Eng Fract Mech 2000;67(6):547–62.
[56] Dodds RH, Ruggieri C, Koppenhoefer K. 3-d effects on models for transferability of cleavage fracture toughness. In: Underwood JH, MacDonald BD, Mitchell MR, editors. Fatigue and fracture mechanics, ASTM STP 1321, vol. 28. Philadelphia: American Society for Testing and Materials; 1997. p. 179–97.
[57] Healy B, Gullerud A, Koppenhoefer K, Roy A, RoyChowdhury S, Petti J, et al. WARP3D: 3-D nonlinear finite element analysis of solids for fracture and fatigue processes. Tech rep. University of Illinois at Urbana-Champaign; 2014. < http://code.google.com/p/warp3d > .
[58] Moran B, Shih CF. A general treatment of crack tip contour integrals. Int J Fract 1987;35:295–310.
[59] Al-Ani AM, Hancock JW. J-dominance of short cracks in tension and bending. J Mech Phys Solids 1991;39:23–43.
[60] Williams ML. On the stress distribution at the base of a stationary crack. J Appl Mech 1957;24:109–14.
[61] Ruggieri C. FRACTUS2D: numerical computation of fracture mechanics parameters for 2-D cracked solids. Tech rep. University of Sao Paulo; 2011.
[62] Miller AG. Review of limit loads of structures containing defects. Int J Press Vessel Pip 1988;32:197–327.
[63] Wolfram Research, Inc.. Mathematica, version 8.0 Edition. Champaign (Illinois): Wolfram Research, Inc.; 2011.
[64] Barbosa VS, Ruggieri C. Fracture toughness testing using non-standard bend specimens – Part II: Experiments and evaluation of T_0 reference temperature for a low alloy structural steel. Eng Fract Mech, https://doi.org/10.1016/j.engfracmech.2018.03.029.